JOURNAL OF COMPUTATIONAL PHYSICS **132,** 34–50 (1997)
ARTICLE NO. CP965593

A Numerical Study of the Effect of Free Surface Deformation on Buoyancy and Thermocapillary Convection

G. Labonia,* F. Stella,* E. Leonardi,† and G. Guj‡

*Dipartimento di Meccanica e Aeronautica, Università di Roma La Sapienza, Rome, Italy; †School of Mechanical and Manufacturing Engineering, The University of New South Wales, Sydney, NSW 2052, Australia; and ‡Dipartimento di Meccanica e Automatica, Terza Università di Roma, Rome, Italy

Received November 10, 1995; revised July 11, 1996

In this paper an improved formulation of the equilibrium equation for the free surface is presented which eliminates the need to evaluate the constant pressure effect. This has then been used in conjunction with a vorticity-velocity formulation discretized using a curvilinear coordinate system in two dimensions. The system of non-linear equations resulting from the discretization of field equations, the free surface displacement, and mesh description are solved simultaneously using Newton's method. This method has been validated using a number of previously reported test cases. The techniques presented have been used to study the effects of free surface deformation and fluid/solid contact angle on combined buoyancy and thermocapillary convection in a steel container filled with water.

1. INTRODUCTION

The effects of surface deformation are neglected in computation of thermocapillary and buoyancy driven flows by the majority of recent works (e.g., Rivas [1, 2] and Babu and Korpela [3]). This hypothesis is justified from the physical point of view when the capillary number is small and in particular when the contact angle (δ) is equal to 0. From the numerical point of view, the condition of a flat free surface is particularly simplifying, permitting the use of a cartesian coordinate system. It is therefore usual to study surface deformations for small capillary numbers (Ca), as a post processing of the known flow field (see, e.g., Rivas [1, 2] and Babu and Korpela [3]).

Much work has been done in steady and transient thermocapillary flows coupling the flow and thermal equations with those of the surface equilibrium in asymptotic theory for an aspect ratio A going to 0 (Sen and Davis [4]), which corresponds to neglecting the inertial terms in the momentum and energy equations at the leading order of approximation. The work of Strani *et al.* [5] reports, in the case of zero gravity, not only asymptotic solutions for A going to 0 but also numerical simulations for general cases at various A and Ca values (see also Sen [6] and Kuhlmann [7]).

In the present work the following aspects have been developed: firstly a mathematical and numerical model is proposed for studying steady two-dimensionally combined thermocapillary and buoyancy induced flows in a variety of different physical and geometrical situations; and then some interesting applications for water at different Marangoni, Bond, and Capillary numbers and contact angles are studied and discussed.

The equations of mass, momentum, energy, and related boundary conditions together with the equations for the equilibrium of the interface have been written in general tensor form. The governing equations are then rewritten as proposed by Guj and Stella [8] in a vorticity-velocity formulation thus eliminating the need to evaluate the pressure. The equilibrium equation for the free surface is rewritten in terms of the surface slope thus eliminating the need to evaluate the constant pressure effect that has to be computed using an integral condition (e.g., Strani *et al.* [5]). All the equations are then discretized by a finite volume (FV) technique in a generalized curvilinear coordinate system which fits the geometry. This geometry can be complex, due either to the prescribed solid walls shape (e.g., a solidification surface) or to free surface deformation (for high Capillary number or contact angle).

All the equations are written in such a way that a simultaneous steady solution for all the variables, including the free surface elevation, is obtained using Newton's method starting from an appropriate initial guess. In this way a variety of complex flow situations can be easily solved and a parametric study can be conducted.

In this paper the applicability of the proposed formulation and the accuracy of the numerical code are evaluated by solving test cases available in the literature (Sen and Davis [4], Strani *et al.* [5], and Behnia *et al.* [10]). Then following the systematic study and categorization of the thermocapillary flows in terms of the non-dimensional groups, results for water (intermediate Prandtl number) in standard and zero gravity situations and small temperature gap are presented and discussed. The importance of the

0021-9991/97 $25.00

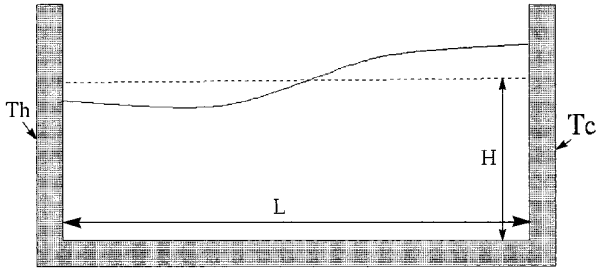

FIG. 1. $2D$ cavity of length L and height H with top free surface.

Marangoni number effect on either the fluid flow and thermal fields or on the elevation of the surface is analyzed. The numerical surface elevation is demonstrated to differ in a significant way from the analytical solution of Sen and Davis [4] for zero contact angle and high Marangoni numbers. It is shown that the contact angle can affect quite significantly the shape of the free surface and the flow and thermal fields in the bulk of the fluid domain for certain physical situations. Finally results confirm that the effect of Capillary number (that is small in the proposed application) is negligible and that the Bond number can affect the shape of free surface as well as flow and thermal fields.

2. MATHEMATICAL FORMULATION

2.1. *Governing Equations*

Consider a rectangular two-dimensional cavity of length L, height H and aspect ratio $A = H/L$, as shown in Fig. 1. It contains a Boussinesq Newtonian liquid of density ρ, dynamic viscosity μ, and thermal diffusivity α. The right wall is maintained at a temperature T_H, the left wall at a temperature T_C, the bottom wall is adiabatic, and the upper surface is a free deformable surface bounded by a passive gas of negligible density and viscosity.

The governing equations for steady state problems are those of the conservation of mass, momentum and energy which are

$$\nabla \cdot \mathbf{u}' = 0 \tag{1}$$

$$\rho \mathbf{u}' \cdot \nabla \mathbf{u}' = -\nabla p' + \mu \nabla^2 \mathbf{u}' - \rho \beta T' \mathbf{g} \tag{2}$$

$$\mathbf{u}' \cdot \nabla T' = \alpha \nabla^2 T' \tag{3}$$

in which $\mathbf{u}$ is the velocity vector, T is the temperature, p is the dynamic pressure, the prime denotes dimensional variables, $\mathbf{g}$ is the gravitational acceleration vector and β is the coefficient of thermal expansion.

2.2. *Interfacial Stress Balance*

On the free surface, which is assumed to be in equilibrium, there is an interfacial stress balance. This results in the following normal and tangential equations at the interface,

$$\sigma' \frac{\partial^2 h'}{\partial \tau'^2} = -p' + \frac{\rho g h'}{\sqrt{1 + (\partial h'/\partial x)^2}} + 2\mu \frac{\partial u_n'}{\partial n'} \tag{4}$$

$$\frac{\partial \sigma'}{\partial \tau'} = \mu \left(\frac{\partial u_\tau'}{\partial n'} + \frac{\partial u_n'}{\partial \tau'} \right) \tag{5}$$

in which h' is the departure of the interface from the free flat surface, and the (τ, n) coordinate system is located on the surface of the interface as shown in Fig. 2. The surface tension σ is assumed to be a linear function of temperature given by

$$\sigma'(T) = \sigma - \gamma(T' - T_R'), \tag{6}$$

where σ and $\gamma = -\partial \sigma'/\partial T'$ are assumed to be constant and evaluated at the reference temperature, T_R'.

To permit the numerical implementation of the determination of the free surface, it is advantageous to manipulate Eq. (4) to avoid the need to evaluate the pressure on the surface by an integral condition (Strani *et al.* [5]). First we differentiate Eq. (4) with respect to τ', and then replace the resulting $-\partial p'/\partial \tau'$ term using the τ' component of the momentum equation on the surface, viz.

$$\frac{\partial p'}{\partial \tau'} = -\rho \frac{\partial}{\partial \tau'} \left(\frac{u_\tau'^2}{2} \right) - \mu \frac{\partial \omega'}{\partial n'} - \rho \beta g (T' - T_R') \left(\frac{\mathbf{g}}{g} \cdot \boldsymbol{\tau} \right), \tag{7}$$

where $\omega' = -\partial u_\tau'/\partial \tau'$ ($u_n' = 0$ on the surface).

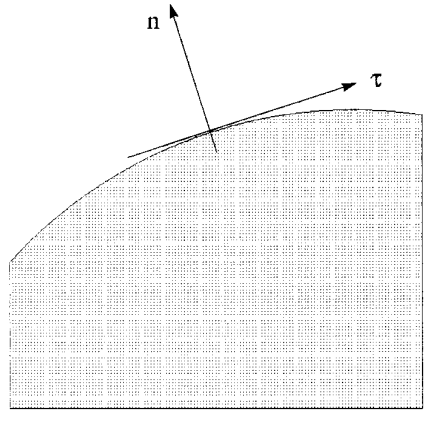

FIG. 2. Coordinate system on free surface.

Thus Eq. (7) yields after some manipulation the final form of the interfacial stress balance equation:

$$\frac{\partial}{\partial \tau'}\left([\sigma-\gamma(T'-T'_R)]\frac{\partial^2 h'}{\partial \tau'^2}\right)-\rho\frac{\partial}{\partial \tau'}\left(\frac{u'^2_\tau}{2}\right)+\mu\left(2\frac{\partial^2 u'_\tau}{\partial \tau'^2}-\frac{\partial \omega'}{\partial n'}\right)-\rho g\frac{\partial h'}{\partial \tau'}-\rho\beta g(T'-T'_R)\left(\frac{\mathbf{g}}{g}\cdot\boldsymbol{\tau}\right)=0. \quad (8)$$

2.3. *Non-dimensionalisation*

The governing equations have been non-dimensionalised using the following scaling variables

$$\mathbf{x}=\mathbf{x}'/L$$
$$u=u'/u_*$$
$$\vartheta=(T'-T_c)/(T_H-T_C)$$
$$p=p'/p_*$$

in which u_* and p_* represent suitable scaling for the velocity and pressure yet to be defined. The conservation equations (1)–(3) thus become

$$\nabla\cdot\mathbf{u}=0 \quad (9)$$

$$\mathbf{u}\cdot\nabla\mathbf{u}=-M_1\nabla p+M_2\nabla^2\mathbf{u}-M_3\vartheta\frac{\mathbf{g}}{g} \quad (10)$$

$$\mathbf{u}\cdot\nabla\vartheta=E_1\nabla^2\vartheta \quad (11)$$

while the surface equilibrium equations are

$$\frac{\partial}{\partial\tau}\left([1-N_1\vartheta]\frac{\partial^2 h}{\partial\tau^2}\right)-N_2\frac{\partial}{\partial\tau}\left(\frac{u_\tau^2}{2}\right)+N_3\left(2\frac{\partial^2 u_\tau}{\partial\tau^2}-\frac{\partial\omega}{\partial n}\right)-N_4\frac{\partial h}{\partial\tau}-N_5\vartheta\left(\frac{\mathbf{g}}{g}\cdot\boldsymbol{\tau}\right)=0 \quad (12)$$

$$\left(\frac{\partial u_\tau}{\partial n}+\frac{\partial u_n}{\partial\tau}\right)=-T_1\frac{\partial\vartheta}{\partial\tau}, \quad (13)$$

where M_i, E_1, N_j, T_1 ($i = 1, 3$, $j = 1, 5$) are ten non-dimensional groups which can be expressed as a combination of the five independent non-dimensional groups as shown in Table I.

TABLE I

Non-dimensional Groups for Different Scaling Velocities

Name	Group	$u_*=\frac{\alpha}{L}$	$u_*=\frac{\nu}{L}$	$u_*=\frac{\lvert\gamma\rvert\Delta T}{\mu}$
M_1	$\frac{P_*}{\rho u_*^2}$	1	1	1
M_2	$\frac{\mu}{\rho L u_*}$	Pr	1	$\frac{Pr}{Ma}$
M_3	$\frac{gL\beta\Delta T}{u_*^2}$	$GrPr^2$	Gr	$\frac{GrPr}{Ma^2}$
E_1	$\frac{\alpha}{Lu_*}$	1	$\frac{1}{Pr}$	$\frac{1}{Ma}$
N_1	$\frac{\lvert\gamma\rvert\Delta T}{\sigma}$	Ca	Ca	Ca
N_2	$\frac{\rho u_*^2 L}{\sigma}$	$\frac{Ca}{MaPr}$	$\frac{CaPr}{Ma}$	$\frac{CaMa}{Pr}$
N_3	$\frac{\mu u_*}{\sigma}$	$\frac{Ca}{Ma}$	$\frac{CaPr}{Ma}$	Ca
N_4	$\frac{\rho g L^2}{\sigma}$	Bo	Bo	Bo
N_5	$\frac{\rho\beta g\Delta TL^2}{\sigma}$	$\frac{CaGrPr}{Ma}$	$\frac{CaGrPr}{Ma}$	$\frac{CaGrPr}{Ma}$
T_1	$\frac{\lvert\gamma\rvert\Delta T}{\mu u_*}$	Ma	$\frac{Ma}{Pr}$	1

Three common choices for the velocity scale which have appeared in the literature are $u_* = \alpha/L$ (conduction equal convection), $u_* = \nu/L$ (low buoyancy), and $u_* = |\gamma|\,\Delta T/\mu$ (Marangoni flows). The last velocity scale gives the advantage that no parameters appear in the boundary conditions when the interface is flat. The other forms yield non-dimensional groups in the tangential stress condition, which may result in ill-conditioned boundary conditions for extreme values of the Marangoni number (Ostrach [11]). These three different non-dimensionalisation schemes have been summarized in Table I, where

$$Pr=\frac{\nu}{\alpha},\qquad Ma=\frac{\gamma\Delta TL}{\mu\alpha},\qquad Gr=\frac{g\beta\Delta TL^3}{\nu^2},$$
$$Ca=\frac{\gamma\Delta T}{\sigma},\qquad Bo=\frac{\rho gL^2}{\sigma}$$

are the Prandtl, Marangoni, Grashof, Capillary and Bond numbers, respectively. The reference velocity $u_* = |\gamma|\,\Delta T/\mu$ has been used throughout this study unless differently specified.

2.4. *Vorticity-Velocity Formulation*

The vorticity ω defined as

$$\boldsymbol{\omega}=\nabla\times\mathbf{u} \quad (14)$$

is introduced in the governing equations to eliminate the pressure as a solution variable. Taking the curl of the momentum equation and of the definition of the vorticity, the vorticity transport equation and kinematic relation between the vorticity and velocity are obtained, viz.

$$\nabla \cdot (\omega \mathbf{u}) = \mathbf{M_2}\, \nabla^2 \omega - \mathbf{M_3}\, \nabla \times \left(\vartheta \frac{\mathbf{g}}{g} \right) \tag{15}$$

$$\nabla^2 \mathbf{u} = -\nabla \times \boldsymbol{\omega}. \tag{16}$$

3. BOUNDARY CONDITIONS

All boundaries of the enclosure (Fig. 1), except the top free surface, are assumed to be solid, impermeable, and at rest. The velocity boundary conditions on the rigid walls are

$$\mathbf{u} = 0 \tag{17}$$

while the velocity boundary conditions on the free surface are Eq. (13) for the tangential component u_τ, and $u_n = 0$, for the normal component. The boundary conditions for vorticity are obtained directly from the definition of the vorticity (eq. (14)) for all the boundaries.

The temperature boundary conditions are

$$\frac{\partial \vartheta}{\partial n} = 0 \tag{18}$$

on the adiabatic bottom wall as well as on the top free surface, where n is the normal direction and

$$\begin{aligned} \vartheta &= 1 \\ \vartheta &= 0 \end{aligned} \tag{19}$$

on the isothermal vertical walls (see Fig. 1).

The three boundary conditions for the surface deformation (Eq. (12)) are

$$\frac{\partial h}{\partial \tau} = \tan \delta$$

on the vertical walls, and

$$\int_0^1 h \, dx = 0$$

from the mass conservation.

4. NUMERICAL MODEL

4.1. *Coordinate System*

The governing equations ((11)–(13) and (15)–(16)) are discretized using a finite-volume approximation on a nonuniform mesh. We use a system of generalized coordinates ξ^i ($i = 1, 2$) in the physical plane, where the interface coincides with a coordinate line. J, $\mathbf{g}^1$, $\mathbf{g}^2$ are respectively the Jacobian and the rows of the transformation matrix $\partial \mathbf{x}/\partial \xi_i$ at the center of the control volume.

4.2. *Discretization Scheme*

The staggering of the variable location is chosen not only to obtain the maximum accuracy of the discretized derivatives but also to ensure the discrete conservation of mass, vorticity, and thermal energy. As discussed by Guj and Stella [8], it is possible to obtain mass conservation, to round-off error, if the horizontal velocity u is located at the middle of the vertical face of the computational cell and the vertical velocity v is located at the middle of horizontal face. Similarly, conservation of vorticity is achieved if ω is located on nodal points, and conservation of thermal energy if ϑ is located at the center of the computational cell. We assume that the two-dimensional domain Ω can be discretized into a group of quadrilaterals. The vertices, centers and midpoints of the edges of the quadrilateral are denoted by $\mathbf{x}_{i,j}$, $\mathbf{x}_{i+1/2,j+1/2}$, $x_{i+1/2,j}$ (or $\mathbf{x}_{i,j+1/2}$), respectively, and $\omega_{i,j}$ is stored on $\mathbf{x}_{i,j}$, $u_{i,j}$ on $\mathbf{x}_{i,j-1/2}$, $v_{i,j}$ on $\mathbf{x}_{i-1/2,j}$, and $\vartheta_{i,j}$ on $\mathbf{x}_{i-1/2,j-1/2}$.

After some manipulation each equation is integrated over an appropriate control volume which depends on the equation that has to be discretized (see Fig. 3) and the Gauss divergence theorem is then applied. We obtain

$$A_k \oint_{\Gamma_{ij}} (\psi, \chi) \cdot \mathbf{n} \, dl = B_k \oint_{\Gamma_{ij}} \nabla \phi \cdot \mathbf{n} \, dl + C_k \int\int_{\Omega_{ij}} \mathscr{Q} \, d\Omega, \tag{20}$$

where

$$\phi = \begin{Bmatrix} \omega \\ J(ug_x^1 + vg_y^1) \\ J(ug_x^2 + vg_y^2) \\ \vartheta \end{Bmatrix}, \qquad \psi = \begin{Bmatrix} u\omega \\ 0 \\ 0 \\ u\vartheta \end{Bmatrix},$$

$$\chi = \begin{Bmatrix} v\omega \\ 0 \\ 0 \\ v\vartheta \end{Bmatrix}, \qquad \mathscr{Q} = \begin{Bmatrix} \partial\vartheta/\partial x \\ \partial\omega/\partial\xi^2 \\ \partial\omega/\partial\xi^2 \\ 0 \end{Bmatrix}.$$

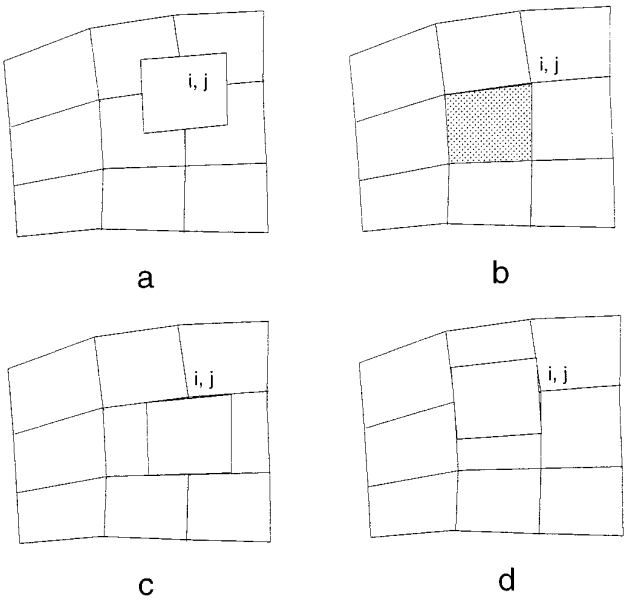

FIG. 3. Control volumes for the equations associated to ω, ϑ, u, and v, respectively.

Γ_{ij} is the boundary of Ω_{ij} and $\mathbf{n}$ is the outward drawn unit normal.

Using the nomenclature shown in Fig. 4, the general form of the convective terms becomes

$$\oint_{\Gamma_{ij}} (\psi, \chi)\cdot \mathbf{n}\, dl \simeq (\psi_e\, \Delta y_{12} - \chi_e\, \Delta x_{12}) + (\psi_n\, \Delta y_{23} - \chi_n\, \Delta x_{23}) + (\psi_w\, \Delta y_{34} - \chi_w\, \Delta x_{34}) + (\psi_s\, \Delta y_{41} - \chi_s\, \Delta x_{41}).$$

A finite-volume discretization is also used to compute the diffusion terms. In this case appropriate values of the gradients of ϕ on the cell faces need to be obtained. We use the expression on $\nabla\phi$ in general coordinates and obtain (see Fig. 4)

$$\begin{aligned}\oint_{\Gamma_{ij}} \nabla\phi\cdot\mathbf{n}\, dl \simeq\ & \{(\phi_E - \phi_p)[(\Delta x_{12})^2 + (\Delta y_{12})^2] \\ & - (\phi_2 - \phi_1)[\Delta x_{12}\,\Delta x_{PE} + \Delta y_{12}\,\Delta y_{PE}]\}/J_e \\ & + \{(\phi_N - \phi_P)[(\Delta x_{23})^2 + (\Delta y_{23})^2] \\ & - (\phi_3 - \phi_2)[\Delta x_{23}\,\Delta x_{PN} + \Delta y_{23}\,\Delta y_{PN}]\}/J_n \\ & + \{(\phi_W - \phi_P)[(\Delta x_{34})^2 + (\Delta y_{34})^2] \\ & - (\phi_4 - \phi_3)[\Delta x_{34}\,\Delta x_{PW} + \Delta y_{34}\,\Delta y_{PW}]\}/J_w \\ & + \{(\phi_S - \phi_P)[(\Delta x_{41})^2 + (\Delta y_{41})^2] \\ & - (\phi_1 - \phi_4)[\Delta x_{41}\,\Delta x_{PS} + \Delta y_{41}\,\Delta y_{PS}]\}/J_s,\end{aligned}$$

where

$$J_e = \Delta y_{12}\,\Delta x_{PE} + \Delta y_{PE}\,\Delta x_{12} \qquad J_n = \Delta y_{23}\,\Delta x_{PN} + \Delta y_{PN}\,\Delta x_{23}$$
$$J_w = \Delta y_{34}\,\Delta x_{PW} + \Delta y_{PW}\,\Delta x_{34} \qquad J_s = \Delta y_{41}\,\Delta x_{PS} + \Delta y_{PS}\,\Delta x_{41}$$

and

$$J(ug_x^1 + vg_y^1) = u\,\Delta y_{sn} - v\,\Delta x_{sn}$$
$$J(ug_x^2 + vg_y^2) = v\,\Delta x_{we} - u\,\Delta y_{we}.$$

In the last term of (20), $\mathcal{Q}$ has been considered constant in the control volume, yielding

$$\int\int_{\Omega_{ij}} \mathcal{Q}\, d\Omega = \Omega_{ij}\mathcal{Q}_P,$$

where for $\mathcal{Q}_P$ we have

$$\left(2\Omega_{ij}\frac{\partial\vartheta}{\partial x}\right)_P = [(\vartheta_2 - \vartheta_4)\,\Delta y_{13} - (\vartheta_3 - \vartheta_1)\,\Delta y_{42}]$$

$$\left(\frac{\partial\omega}{\partial\xi^1}\right)_P = (\omega_e - \omega_w)$$

$$\left(\frac{\partial\omega}{\partial\xi^2}\right)_P = (\omega_n - \omega_s).$$

The unknowns for the problem are not prescribed at all the focal points (see the sketch of the computational molecule); so a bilinear interpolation has been adopted for evaluating the unknowns where needed.

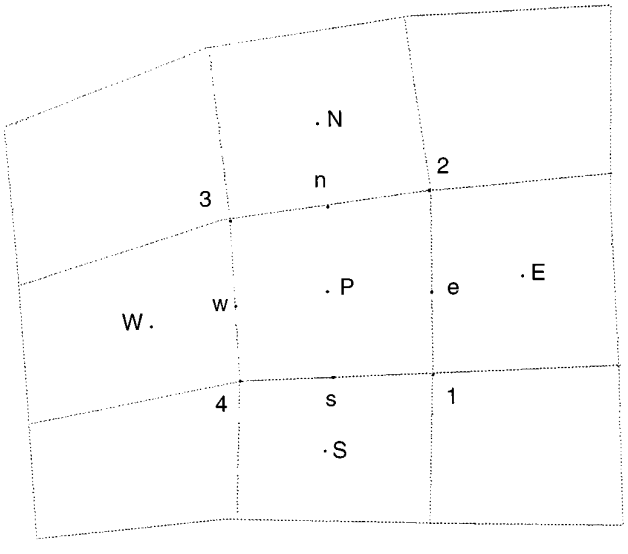

FIG. 4. Computational molecule notation.

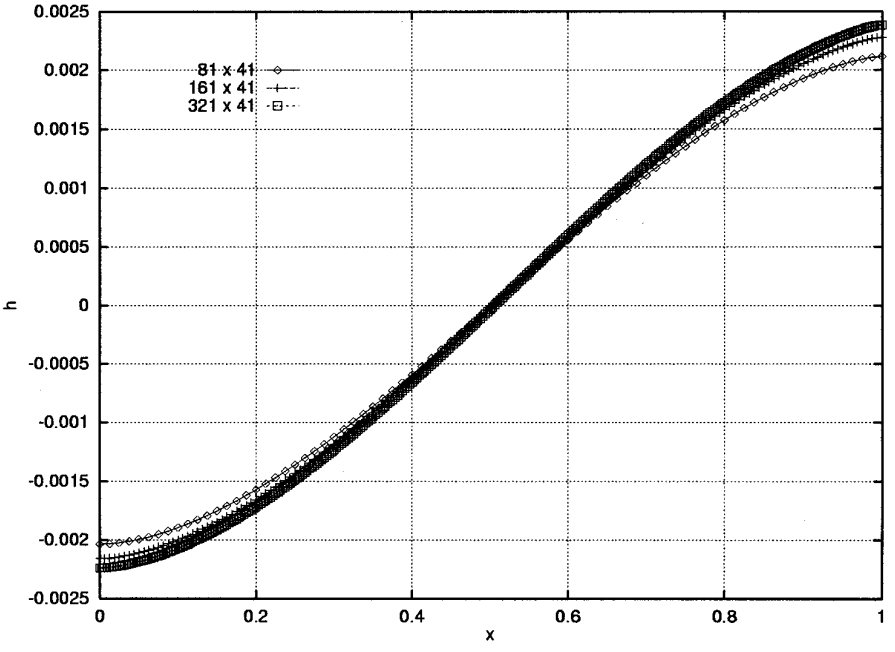

FIG. 5. Mesh sensitivity analysis for the surface elevation at $Pr = 6.95$, $Ma = 5200$, $Ca = 0.01$, $Bo = Gr = 0$, $A = 0.2$.

4.3. *Method of Solution*

4.3.1. *Newton's Method.* The system of non-linear equations described in the previous section can be symbolically written as

$$\mathbf{f}(x) = \mathbf{0}, \tag{21}$$

where $\mathbf{f}$ includes field equations written for the entire solution domain, the boundary conditions and equations for the evaluation of the free surface displacement. $\mathbf{x}$ is a possible solution which includes the vorticity, two velocity components and temperature in the entire domain, and the surface displacement slope $(\partial h/\partial \tau)$ on the free boundary. Furthermore when the free surface deformation is also included in the model, x also incorporates the grid coordinates (τ, n) and $\mathbf{f}$ incorporates the algebraic equation for the evaluation of τ and n from the surface deformation h. In this way Newton's method permits the simultaneous solution of all the variables.

Newton's iteration is obtained in the usual way by considering a linearization of the problem on an initial guess $\mathbf{x_o}$ for $\mathbf{x}$

$$\mathbf{f}(\mathbf{x_o}) + \left.\frac{\partial \mathbf{f}}{\partial \mathbf{x}}\right|_{\mathbf{x_o}} \Delta\mathbf{x} = \mathbf{0} \tag{22}$$

yielding

$$\left.\frac{\partial \mathbf{f}}{\partial x}\right|_{\mathbf{x_o}} \Delta\mathbf{x} = -\mathbf{f}(\mathbf{x_o}). \tag{23}$$

The Jacobian matrix $\mathbf{J} = \partial \mathbf{f}/\partial x$ represents the sensitivity of the initial vector to changes in the solution. The successive approximations for $\mathbf{x}$ are obtained using

$$\mathbf{x_{n+1}} = \mathbf{x_n} + \Delta\mathbf{x}. \tag{24}$$

4.3.2. *Jacobian Evaluation.* Evaluation of the Jacobian matrix can be obtained either analytically or numerically. The analytical evaluation is obviously possible but difficult especially when the problem has such a large dimension and complexity. In the present paper a numerical evaluation of $\mathbf{J}$ has been preferred. This procedure requires only the evaluation of the residual function $\mathbf{f}(\mathbf{x})$ and is computationally very simple. The Jacobian $\mathbf{J}$ is approximated using

$$\frac{\partial f_i}{\partial x_j} \approx \frac{f_i(\mathbf{x} + \varepsilon \mathbf{e}_j) - f_i(\mathbf{x} - \varepsilon \mathbf{e}_j)}{2\varepsilon} \tag{25}$$

in which $\mathbf{e}_j$ is a unity vector in the j direction (i.e., it has zero on all the components except on the jth that is 1) and ε is a small quantity suitable for numerical differentiation (we have determined using numerical experimentation that 10^{-3} is a good value). It is obvious that a straightforward implementation of Eq. (23) requires $2N_{eq}^2$ (where N_{eq} is the number of equations solved) evaluations of $\mathbf{f}(\mathbf{x})$, with

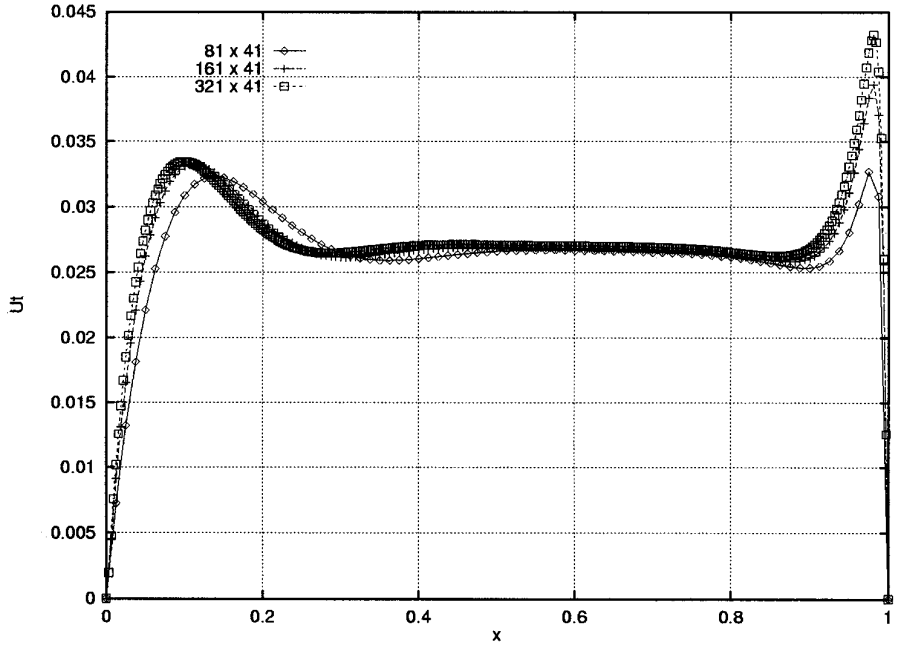

FIG. 6. Mesh sensitivity analysis for the u_τ at $Pr = 6.95$, $Ma = 5200$, $Ca = 0.01$, $Bo = Gr = 0$, $A = 0.2$.

a consequent prohibitive computational cost. However, since the sparsity pattern of **J** is known, its economical evaluation can be performed for the elements that are non-zero. This significantly reduces the computational costs.

4.3.3. *Solution of the Linear System.* For the solution of the linear set of equations (23) a preconditioned *Bi − CGStab* technique (Stella and Bucchignani [9]) has been adopted. *Bi − CGStab* is a suitable method for solving sparse linear systems such as those generated by finite volume techniques applied to computational fluid dynamics.

Incomplete LU factorization with zero fill-in ($ILU(0)$) has been chosen as a preconditioner. *ILU* factorization requires the generation of a lower (L) and upper (U) triangular factorization. This can be obtained by writing a variant of the Crout factorization algorithm. Only the elements that originally are non-zero in the matrix **J** are evaluated and stored in LU factorization; the other elements are assumed to be zero. This avoids the generation of non-zero elements in the bandwidth of the matrix, so that L and U factors have the same sparsity pattern of the original matrix **J** with an enormous saving in both CPU time and memory requirements.

4.3.4. *Stability of the Steady Solutions.* Since the goal of the present method is to find steady solutions using a fast numerical technique, we adopted a Newton Method suitable for finding a steady state solution. A true transient variant of the method has been adopted only to verify *a posteriori* the stability of the solutions.

The time has been non-dimensionalised using $t_* = u_*/L$ as a scaling variable, then the time-dependent form of the conservation equations (11)–(15) becomes

$$\vartheta_t + \mathbf{u} \cdot \nabla \vartheta = E_1 \nabla^2 \vartheta \tag{26}$$

$$\omega_t + \nabla \cdot (\omega \mathbf{u}) = \mathbf{M_2} \nabla^2 \omega - \mathbf{M_3} \nabla \times \left(\vartheta \frac{\mathbf{g}}{g} \right). \tag{27}$$

Thus, the system of non-linear equations can be symbolically written as

$$\beta \frac{\partial \mathbf{x}}{\partial t} + \mathbf{f}(\mathbf{x}) = \mathbf{0}$$

with $\beta = 0$ except for the discretized form of the field equations (27)–(26) for which $\beta = 1$. Starting from the

TABLE II

Mesh Sensitivity Analysis

Variable	81 × 41	161 × 41	321 × 41	n	Extrapolation
h_{min}	$-2.039 \cdot 10^{-3}$	$-2.162 \cdot 10^{-3}$	$-2.226 \cdot 10^{-3}$	0.96	$2.293 \cdot 10^{-3}$
v_{max}	$6.646 \cdot 10^{-3}$	$7.053 \cdot 10^{-3}$	$7.144 \cdot 10^{-3}$	2.15	$7.170 \cdot 10^{-3}$
v_{min}	$-6.356 \cdot 10^{-3}$	$-6.763 \cdot 10^{-3}$	$-6.877 \cdot 10^{-3}$	1.83	$-6.922 \cdot 10^{-3}$
$(u_\tau)_{Peak}$	$3.270 \cdot 10^{-2}$	$3.940 \cdot 10^{-2}$	$4.224 \cdot 10^{-2}$	1.24	$4.433 \cdot 10^{-2}$

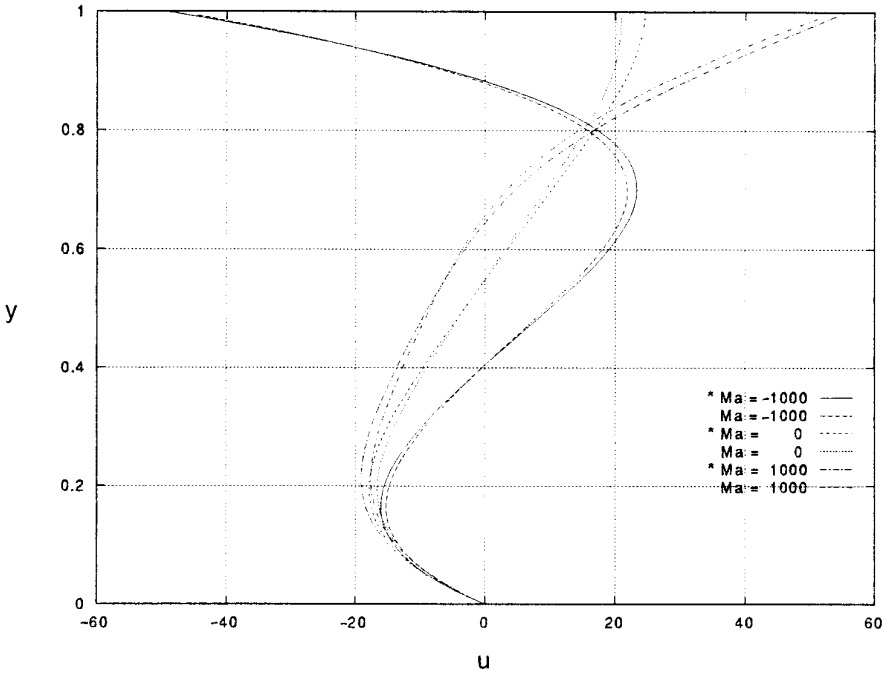

FIG. 7. $u(u_* = \alpha/L)$ velocity profiles in the $x = 0.5$ cavity mid-plane at various Ma and $Pr = 7$, $Gr = 1429$, $A = 1$. * indicates the 3D solution from Behnia *et al.* [10].

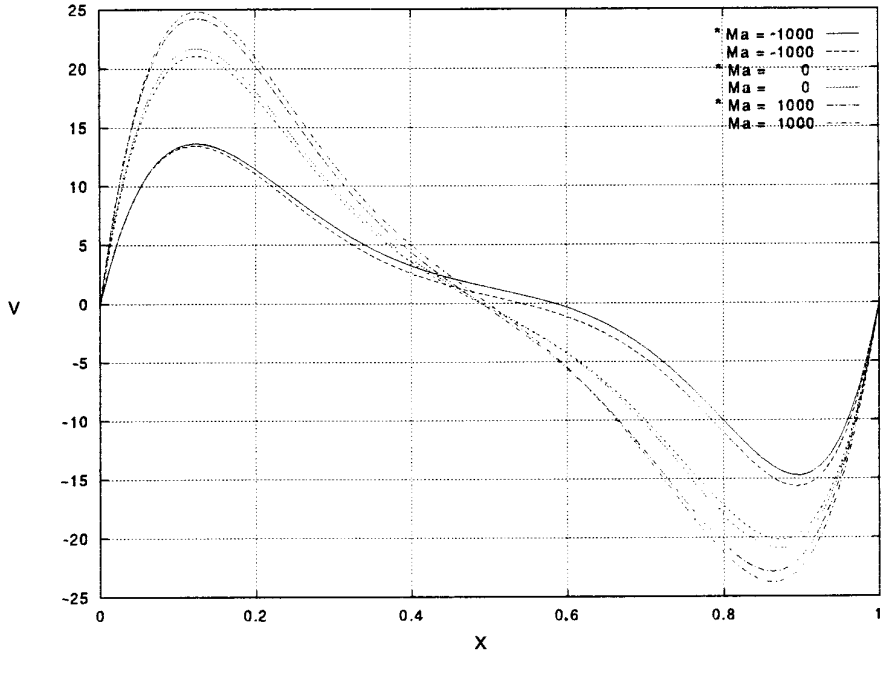

FIG. 8. $v(u_* = \alpha/L)$ velocity profiles in the $y = 0.5$ cavity mid-plane at various Ma and $Pr = 7$, $Gr = 1429$, $A = 1$. * indicates the 3D solution from Behnia *et al.* [10].

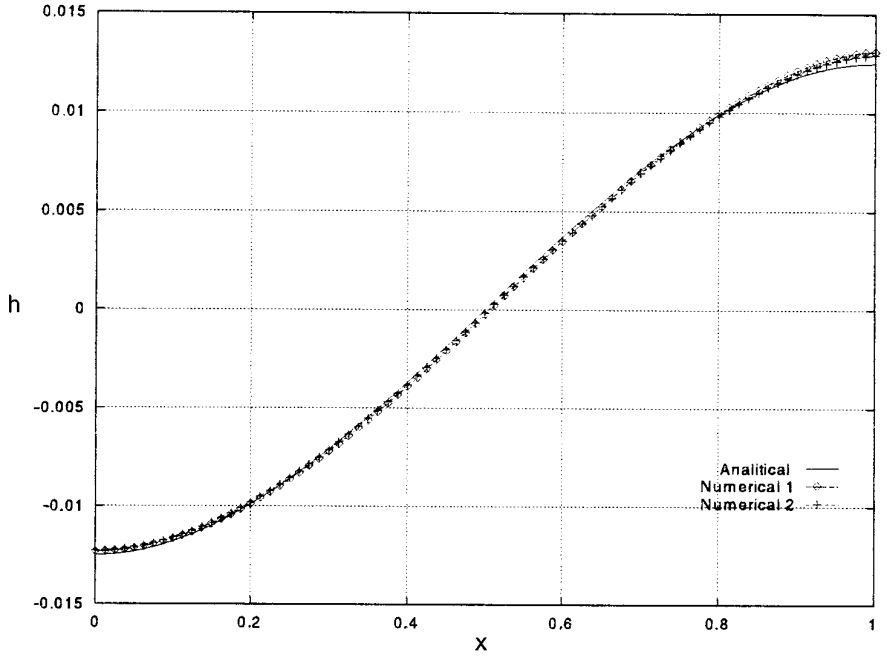

FIG. 9. Surface elevation for $A = 0.2$, $Ma = 5$, $Pr = 0.2$, and $Ca = 0.04$ (case proposed in Sen and Davis [4]). "Numerical 1" is post-processed from the flat condition while "Numerical 2" is explained in Subsection 4.3.

steady solutions, a few time iterations for $\mathbf{x}$ were calculated using a fully implicit scheme,

$$\mathbf{x_{n+1}} = \mathbf{x_n} - \left[\beta \frac{\mathbf{I}}{\Delta t} + \frac{\partial \mathbf{f}}{\partial \mathbf{x}}\bigg|_{\mathbf{x_n}}\right]^{-1} \mathbf{f}(\mathbf{x_n}).$$

For all the results shown, the solution found using this time dependent approach was indistinguishable from the previous stationary one, assuring the stability of the steady solutions.

5. RESULTS

5.1. *Validation of the Numerical Method*

The numerical solutions can be affected by two kinds of errors: discretization errors and consistency errors. First a mesh sensitivity analysis is performed in order to determine the grid spacing requirements for obtaining accurate solutions and to evaluate the convergence order of the discretization scheme. The following values for the dimensionless parameters have been selected as a test case: $Pr = 6.95$, $Ma = 5200$, $Ca = 0.01$, $Bo = Gr = 0$, $A = 0.2$.

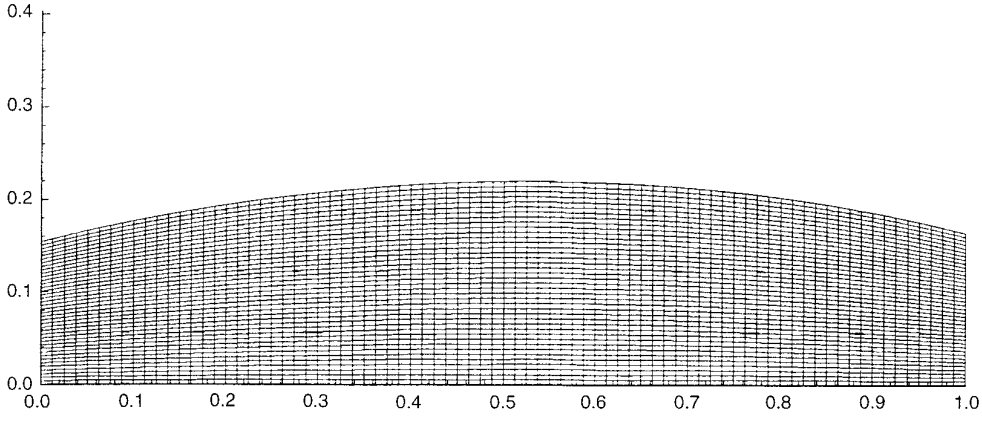

FIG. 10. Mesh used for studying the test case proposed by Piva *et al.* [12].

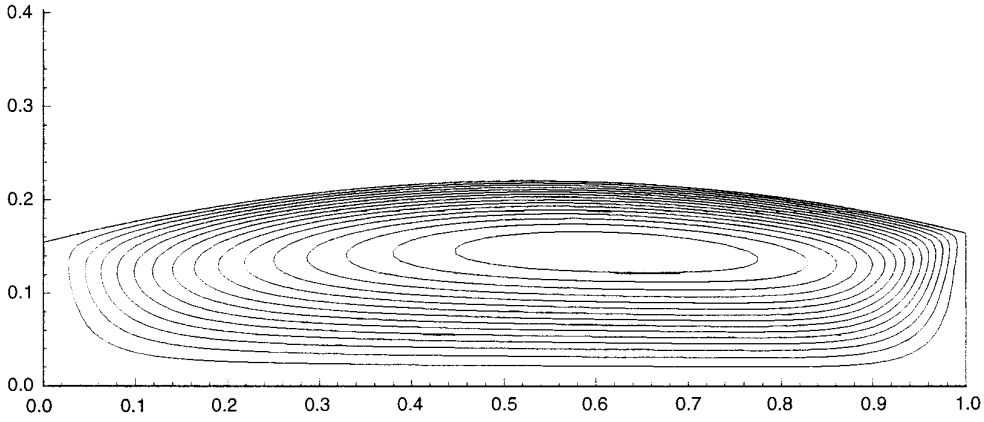

FIG. 11. Streamlines for $Pr = 1$, $Gr = Bo = 0$, $A = 0.2$, $Ca = 0.02$, $Ma = 20$, and $\tan \delta = 0.27$.

Initially three different meshes have been investigated: 41×21, 81×41, and 161×81; these meshes give 4041, 14441, 54441 unknowns, respectively. The analysis of the error between 81×41 mesh results and the extrapolated values obtained by using a Richardson extrapolation for the quantities in the bulk of the domain has shown very good accuracy. The results are not shown here because they are indistinguishable from the 81×41 mesh results. The order of convergence found was approximately equal to two. On the other hand, the resolution of the boundary layer near the lateral walls was not adequate. A second mesh analysis was therefore performed, increasing the number of points in the x direction. Although the numerical procedure is very robust it has large memory requirements and it was therefore necessary to limit the number of mesh points in the y direction to 41. This from the previous analysis was found to be sufficiently accurate. Three meshes were tested: 81×41, 161×41, and 321×41. In Figs. 5 and 6 the effect of mesh on surface deformation, h, and tangential velocity on the free surface, u_τ, is presented. A quantitative mesh sensitivity analysis together with the order of convergence, n, and extrapolated values obtained using a Richardson extrapolation (in the x direction) are presented in Table 2.

The results confirm the finding of the first sensitivity analysis. We found that the method is approximately second-order accurate (x direction) for the internal fields whereas it is first-order accurate for the free surface quantities. This is due to the fact that although the surface equilibrium equation is discretized using a second-order scheme, h appears implicitly in all the equations throughout the grid, since body fitted coordinates have been used. Consequently, by its very nature, h can only be first order. This first order effect is clearly seen in Fig. 5. Further, since the tangential velocity component on the free surface, u_τ, is not a solution variable, but rather is obtained by a linear

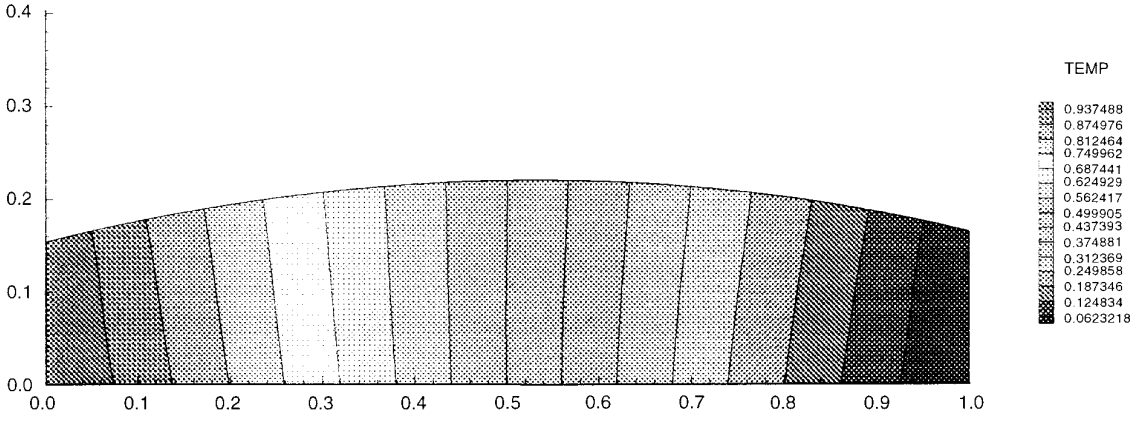

FIG. 12. Isotherms for $Pr = 1$, $Gr = Bo = 0$, $A = 0.2$, $Ca = 0.02$, $Ma = 20$, and $\tan \delta = 0.27$.

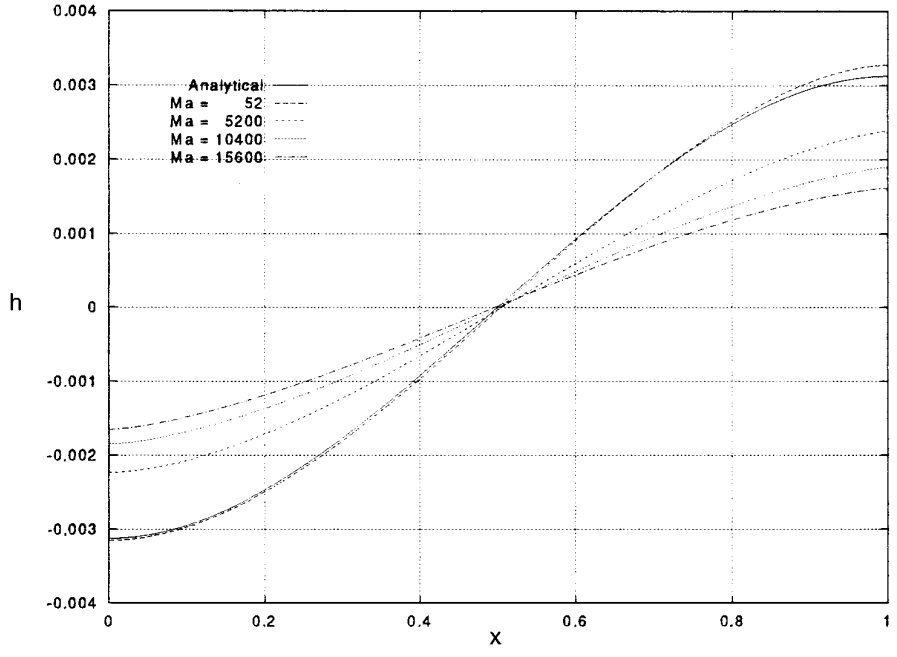

FIG. 13. Surface elevation at various *Ma* with $Gr = Bo = 0$, $Ca = 0.01$, and $\delta = 0°$.

interpolation and a subsequent projection of **u** on the tangent of the free surface (which is first-order) it is not surprisng that this is of order 1.24.

The results discussed above induced us to adopt a 321×41 mesh through all this work.

To examine the second type of errors, the results of the present simulations were compared with Behnia *et al.* [10]. Particularly, for testing the buoyancy and thermocapillary convection, we reproduced three test cases (Figs. 7 and 8) from Behnia *et al.* [10] in which a range of solutions

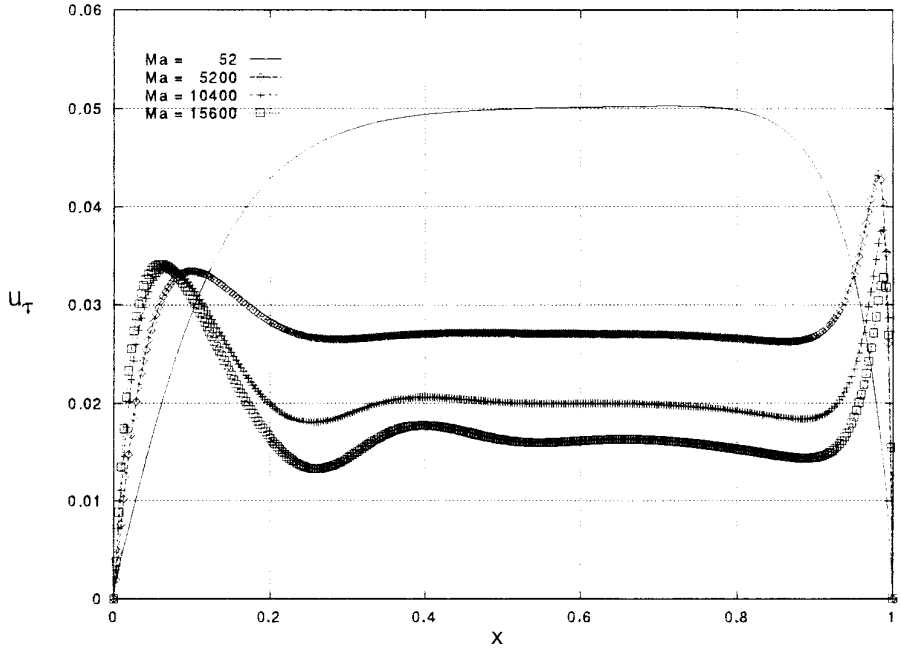

FIG. 14. Tangential velocity (u_τ) on free surface at various *Ma* with $Gr = Bo = 0$, $Ca = 0.01$, and $\delta = 0°$.

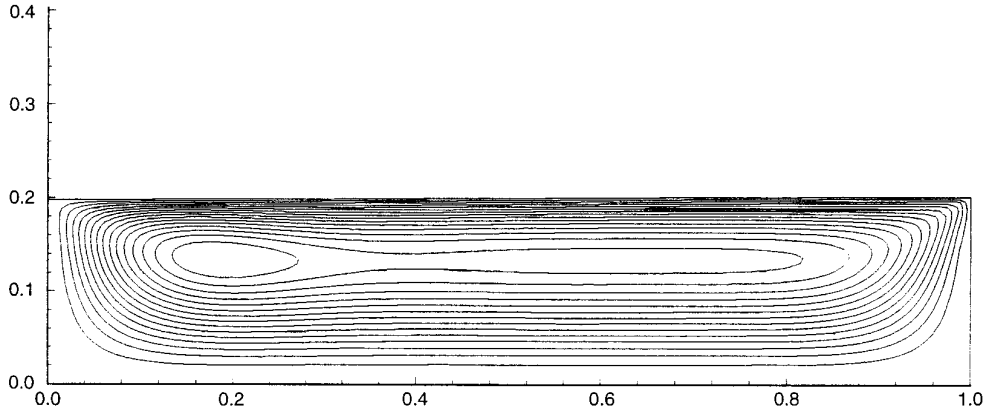

FIG. 15. Streamlines for $Ma = 5200$, $Gr = Bo = 0$, $Ca = 0.01$, and $\delta = 0°$ with $\Delta\psi = 5.49609 \times 10^{-5}$.

was presented for changing Ma. The agreement between the results obtained with the present code (81×81 mesh for the aspect ratio of 1) and those of Behnia *et al.* [10] is very satisfactory. The discrepancies which were observed are due to three-dimensional effects which are not accounted for in the present two-dimensional simulation.

5.2. *Accuracy of Evaluation of the Interface*

Particular attention has to be paid to the validation of the method proposed for evaluating the surface deformation (Eqs. (12) and (13)). The present numerical results have been compared with the analytical solution obtained by Sen and Davis [4]. For zero gravity, small aspect ratio, and neglecting the convective terms in the energy equation, Sen and Davis obtain an analytical expression for the interface shape which is particularly suitable for the present validation. By algebraic manipulation of this expression, the elevation (h) can be written in the following form which is appropriate for an order of magnitude analysis:

$$h = -\frac{1}{16}\frac{Ca}{A}(x - 0.5)(4x^2 - 4x - 2) + \frac{1}{12}\tan\delta(12x^2 - 12x + 2), \tag{28}$$

where δ is the contact angle from the horizontal and x is the projection over the horizontal of the non-dimensional **x** introduced in subsection 2.3.

In Fig. 9 the numerical evaluation of h obtained using an 81×41 mesh is compared to the analytical solution of Sen and Davis [4] with the following parameter values: $A = 0.2$, $Ma = 5$, $Pr = 0.2$, and $Ca = 0.04$. Two numerical methods for determining the surface were tested: ''Numerical 1'' is a post-processing of results obtained using a flat

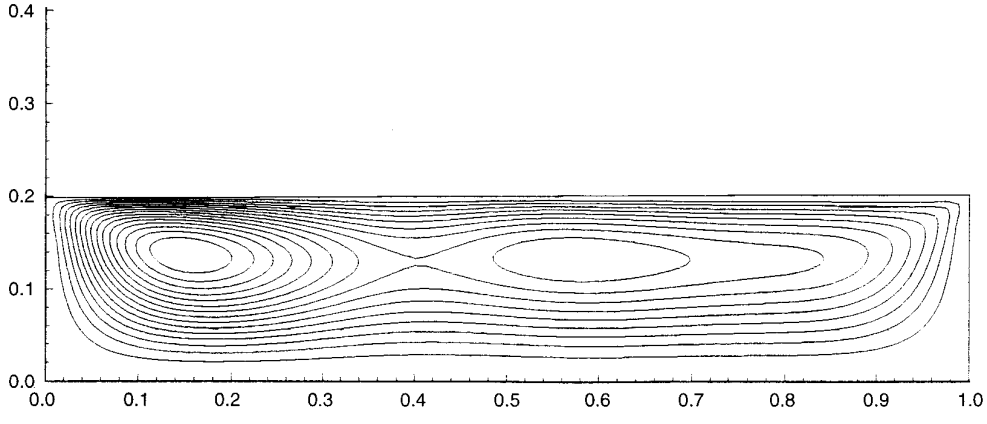

FIG. 16. Streamlines for $Ma = 15600$, $Gr = Bo = 0$, $Ca = 0.01$, and $\delta = 0°$ with $\Delta\psi = 5.24605 \times 10^{-5}$.

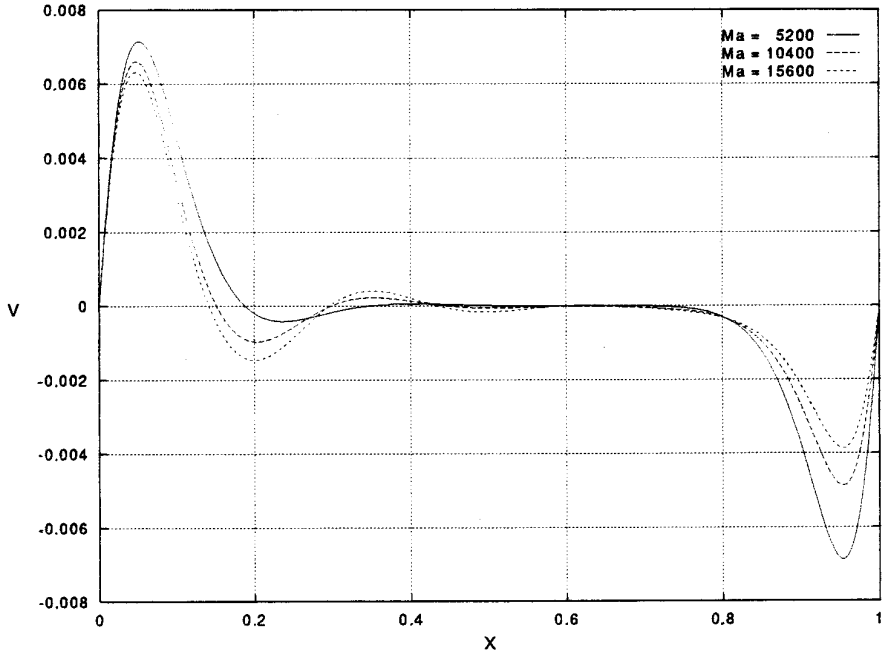

FIG. 17. Vertical velocity in the $y = 0.5$ cavity mid-plane at various Ma with $Gr = Bo = 0$, $Ca = 0.01$, and $\delta = 0°$.

surface condition (as done by Rivas [2]) while "Numerical 2" is using the currently proposed method, in which the interface is obtained by solving implicitly the system resulting from the coupled governing conservation equations and mesh coordinates equations. Both numerical solutions are very close to the analytical $h(x)$ and the difference is negligible.

The last test case is a problem studied by Piva *et al.*

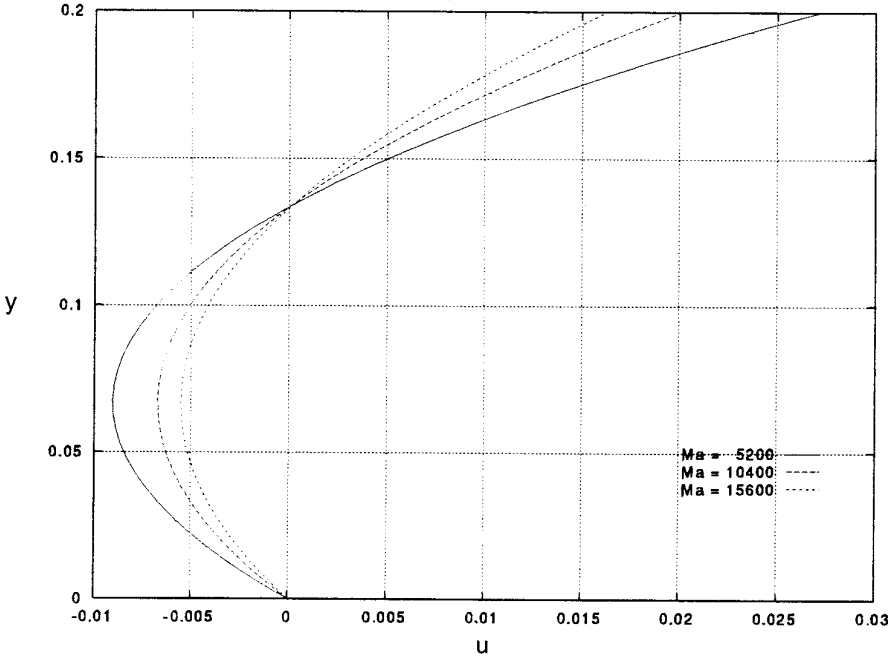

FIG. 18. Horizontal velocity in the $x = 0.5$ cavity mid-plane at various Ma with $Gr = Bo = 0$, $Ca = 0.01$, and $\delta = 0°$.

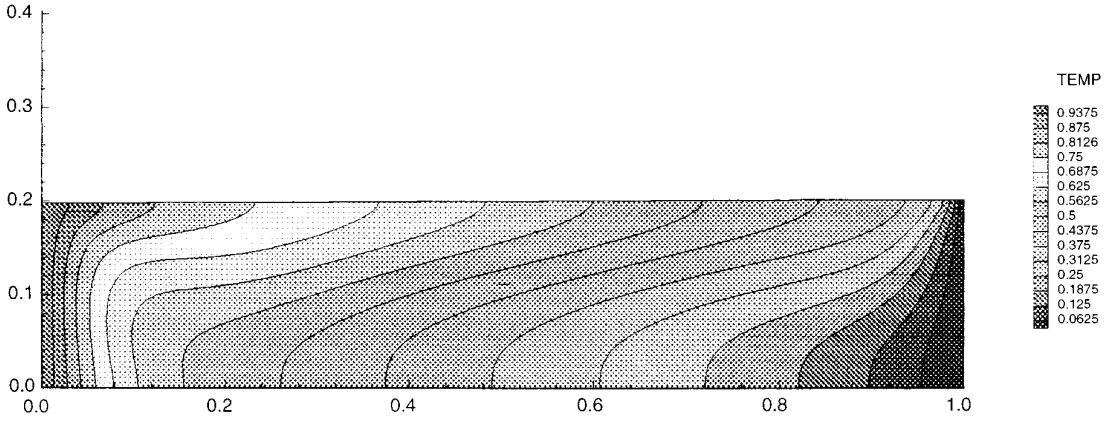

FIG. 19. Isotherms for $Ma = 5200$, $Gr = Bo = 0$, $Ca = 0.01$, and $\delta = 0°$.

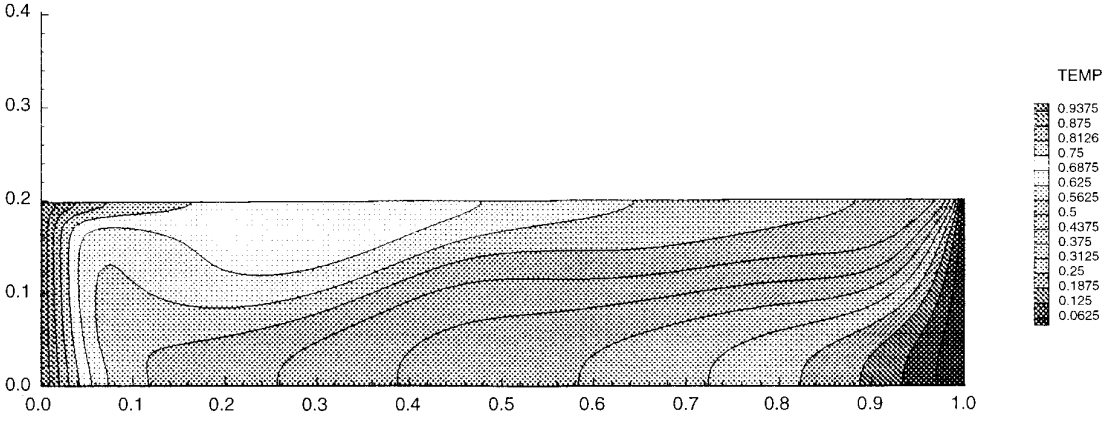

FIG. 20. Isotherms for $Ma = 15600$, $Gr = Bo = 0$, $Ca = 0.01$, and $\delta = 0°$.

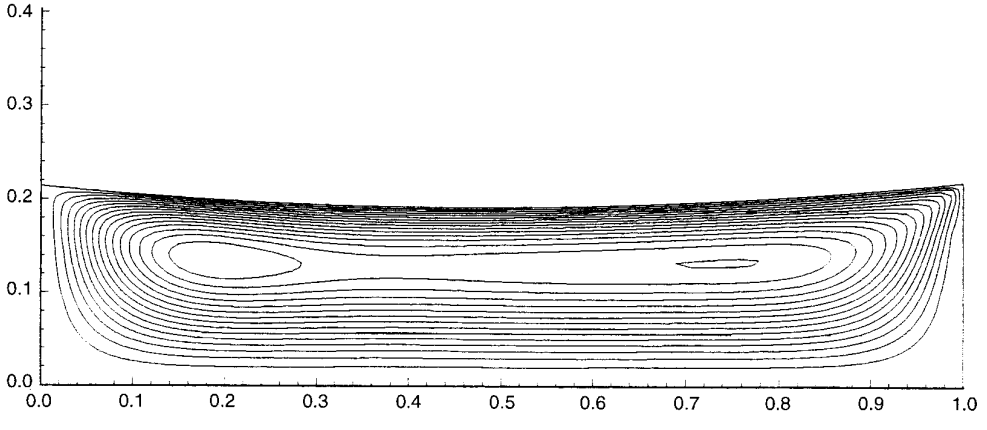

FIG. 21. Streamlines for $\tan \delta = -0.1$ and $Ma = 5200$, $Ca = 0.01$, $Gr = Bo = 0$ with $\Delta\psi = 5.49609 \times 10^{-5}$.

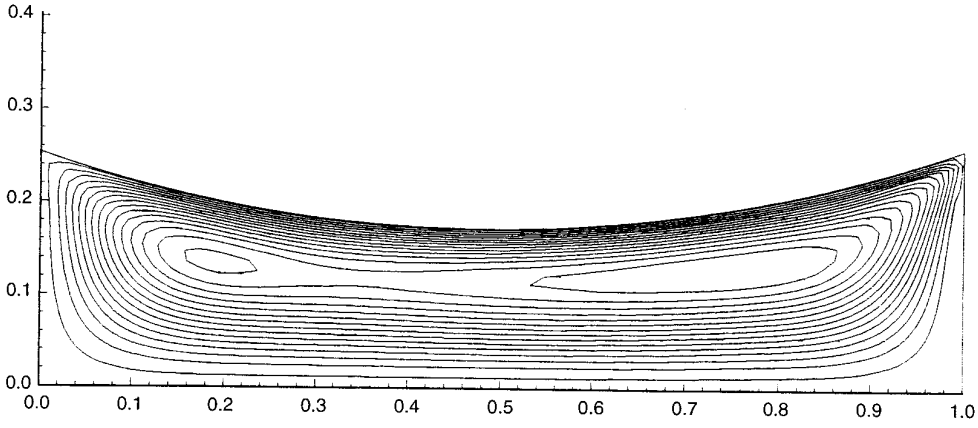

FIG. 22. Streamlines for tan $\delta = -0.35$ and $Ma = 5200$, $Ca = 0.01$, $Gr = Bo = 0$ with $\Delta\psi = 5.49609 \times 10^{-5}$.

[12] for tan δ and Ca values for which large free surface deformations occur. The parameters used are $Pr = 1$, $Gr = Bo = 0, A = 0.2, Ca = 0.02, Ma = 20$, and $\tan\delta = 0.27$. The free surface shape determined using the asymptotic theory (Eq. (28)) and the numerical calculations are indistinguishable from the graphical point of view and so the figure is not shown here (maximum difference equal to 1.8%). The strong effects that large surface deformation has on the streamlines and thermal fields[1] when calculated by our proposed implicit technique can be clearly seen in Figs. 10–12.

We have shown the accuracy of the proposed numerical procedure and the robustness of the implicit solution method.

5.3. *Water Result*

In order to investigate the effects of Marangoni, Capillary, Bond, and Grashof numbers and contact angles on thermocapillary and buoyancy induced flows we have studied the behavior of water ($Pr = 6.95$) in a steel container, with $A = 0.2$ at the averaged temperature of $T'_R = (T_H + T_C)/2 = 20°C$.

First, the effect of Ma on the free surface was investigated. This was achieved by varying the length, L, from 1 to 3 mm for a ΔT of 5°C which corresponds to Ma varying from 5200 to 15600. The other parameters were chosen to be $Gr = Bo = 0$, $Ca = 0.01$, and $\delta = 0°$. The surface deformation is, as expected, negligible with respect to the height of the cavity, but the dependence of $h(x)$ on Ma (Fig. 13) is still significant so that the analytical shape of Sen and Davis [4] cannot be applied at high Ma. This behavior can be explained by considering the tangential velocity on the free surface (Fig. 14). From Eq. (12) it can be shown that $h(x) \propto u_\tau^2 Ma$. It can be seen from Fig. 14 that as Ma is increased this product decreases and consequently the surface deformation decreases too. We have to observe that the effect of the non-linear terms in Eq. (11) gives a growth of a thermal boundary layer close to the right hand wall (Figs. 19 and 20); consequently, from Eq. (13), the kinematical boundary layer near the free surface becomes thinner closer to $x = 1$ and the trend of the superficial tangential velocity (Fig. 14) shows a steep increase followed by rapid decrease for satisfying the boundary condition at $x = 1$. This behavior has been discussed in Strani *et al.* [5]. The intensity of the global recirculation decreases for increasing Ma (Figs. 15 and 16) even if the fluid structures tend to became more complex with the development of a second and third vortex which rotate in the same direction of the single vortex seen in Fig. 11. These behaviors are also exhibited by the profiles of the vertical velocity shown in Fig. 17, and the reduction of the strength of the vortex is confirmed by Fig. 18. Due to an increase in the strength of the left vortex, the isotherms (Fig. 19 and 20) become distorted and the thickness of the thermal boundary layer near the lateral walls is reduced. The hot fluid penetration in the bulk of the domain is enhanced by the strength of the upper left vortex.

If we add the effects of buoyancy forces to those of surface tension, the flow structure does not change. This behavior is expected by an order of magnitude consideration. For the non-dimensional parameters considered, the orders of dependence on the length scale are $Bo \simeq \mathcal{O}(L^2)$, $Gr \simeq \mathcal{O}(L^3)$, but $Ma \simeq \mathcal{O}(L)$. At earth gravity and with $L = 10^{-3}$ m, Bo and Gr ($Gr = 10$ and $Bo = 0.14$) are indeed orders of magnitude less than Ma ($Ma = 5200$).

Next the effects of the contact angle were investigated with $Ma = 5200$, $Ca = 0.01$, $Gr = Bo = 0$, and δ varying

[1] Throughout this study we have used the following convention for the representation of streamlines and isotherms: the streamlines are equally spaced at $\Delta\psi = (\psi_{max} - \psi_{min})/15$; the isotherms are also equally spaced at $\Delta T = (T_H - T_C)/15$.

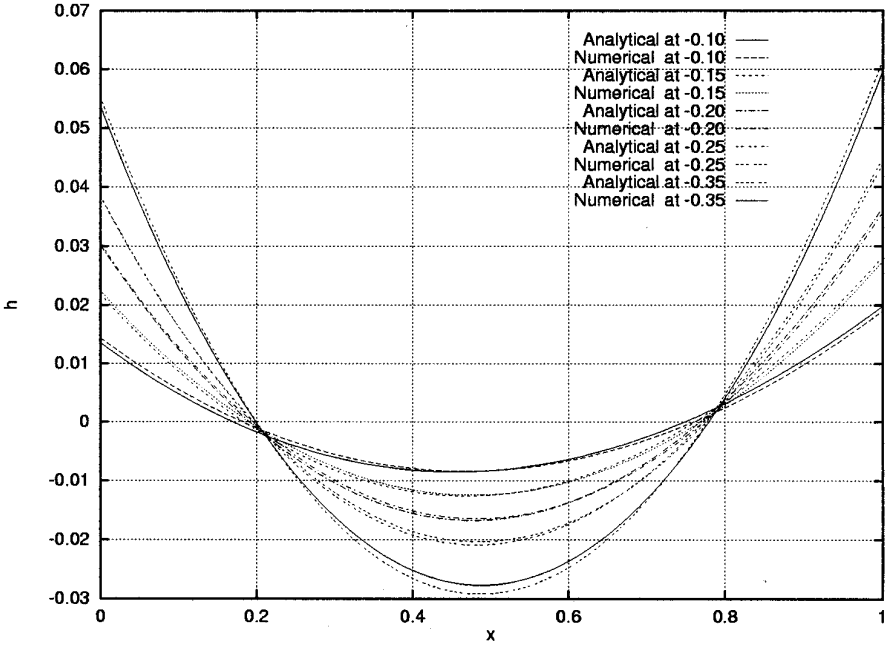

FIG. 23. Surface deformation at various δ with $A = 0.2$, $Ma = 5200$, $Ca = 0.01$, and $Gr = Bo = 0$.

from 0° to −20° (corresponding to possible water-steel contact angles). As shown in Figs. 21 and 22, for decreasing δ a secondary vortex in the upper and right region of the cavity appears and grows, which is different from the one shown in Fig. 15 at $\delta = 0°$. In Fig. 23, numerical and analytical (Eq. (28)) values of $h(x)$ are compared and excellent agreement results. It should be noted that for high δ the analytical solution is not strictly valid; however, the difference between this and the numerical solution is small (see Fig. 23 for $\tan \delta = -0.35$). Although the flow fields

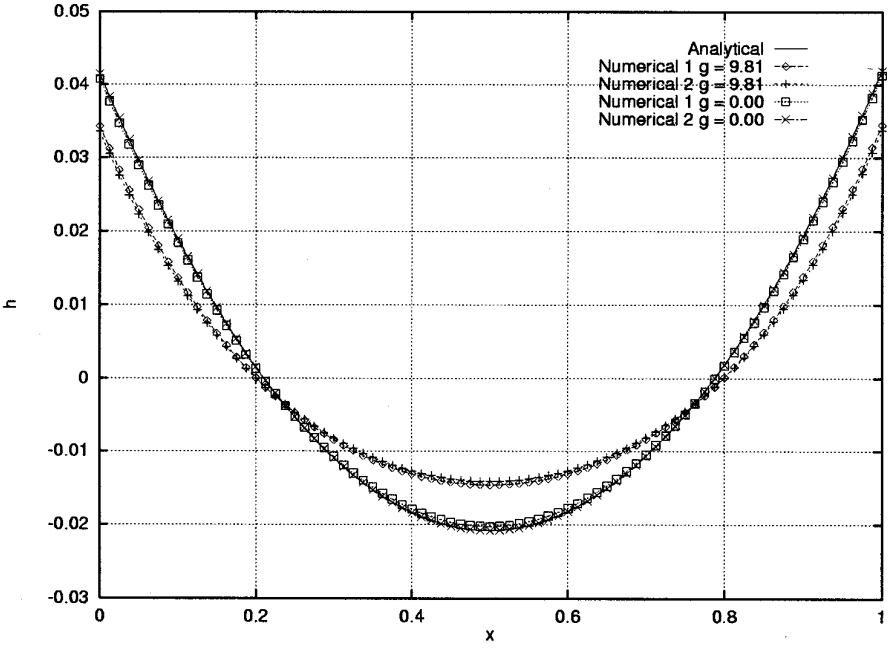

FIG. 24. Effect of gravity on $h(x)$ for $Ma = 5200$, $Ca = 0.001$, $A = 0.2$, and $\tan \delta = -0.25$.

have changed, the thermal gradient within the solution domain is not significantly altered and is therefore not presented here.

The effect of the Marangoni number ($5200 \leq Ma \leq 15600$) has been also studied at $\tan \delta = -0.35$, $Ca = 0.01$ in weightless conditions ($Gr = Bo = 0$). Although the surface deformation had an effect on the flow fields as seen in Fig. 22, varying Ma did not result in any noticeable changes to the free surface. Variation of Ma resulted in a change in the flow structure similar to that seen in Figs. 15 and 16, and the thermal fields obtained are similar to those observed for a contact angle of 0° (see Figs. 19 and 20).

As discussed above, the effect of gravity (Bo) on the surface is of order L^2 and so a container with $L = 10^{-2}$ m has been selected to study such an effect; hence ΔT has been chosen to be 0.5°C to maintain the $Ma = 5200$ ($Ca = 0.001$). The significant effect of gravity on the surface elevation can be seen in Fig. 24.

Finally we have studied the influence of Ca in water-steel cases. The numerical results, not presented, confirm what was expected from an order of magnitude analysis of the terms in Eq. (28); that is, the effect of Ca in water with $\Delta T < 10$°C is negligible.

6. CONCLUSIONS

An original method based on the finite volume technique is proposed for solving buoyancy and thermocapillary convection. The robustness and accuracy is a consequence of the application of a direct, steady state solver based on Newton iteration. The solution for low and intermediate Ca is validated using available results. The method has been applied to study the behavior of water in a steel container for $5200 \leq Ma \leq 15600$ and for earth and zero gravity values and different contact angles. The effect of Ma is significant only at $\delta = 0°$, whereas the gravity effects (Bo) become important at high contact angles.

REFERENCES

1. D. Rivas, High-Reynolds-number thermocapillary flows in shallow enclosures, *Phys. Fluids A* **3,** 280 (1991).
2. D. Rivas, Viscous effects on the free surface deformation in thermocapillary flows, *Phys. Fluids A* **3,** 2466 (1991).
3. V. Babu and S. A. Korpela, Three-dimensional thermocapillary convection in a cavity, *Comput. Fluids* **18,** 229 (1990).
4. A. K. Sen and S. H. Davis, Steady thermocapillary flows in two-dimensional slots, *J. Fluid Mech.* **121,** 163 (1982).
5. M. Strani, R. Piva, and G. Graziani, Thermocapillary convection in a rectangular cavity: Asymptotic theory and numerical simulation, *J. Fluid Mech.* **130,** 347 (1983).
6. A. K. Sen, Thermocapillary convection in a rectangular cavity with deformable interface, *Phys. Fluids* **29,** 3881 (1986).
7. H. Kuhlmann, Small amplitude thermocapillary flow and surface deformations in a liquid bridge, *Phys. Fluids A* **1,** 672 (1989).
8. G. Guj and F. Stella, Numerical solution of high-*Re* recirculating flows in vorticity-velocity form, *Int. J. Numer. Methods Fluids* **8,** 405 (1988).
9. F. Stella and E. Bucchignani, A true transient vorticity-velocity method using preconditioned Bi-CGSTAB, *Numerical Heat Transfer Part B,* **30,** 315 (1996).
10. M. Behnia, F. Stella, and G. Guj, Buoyancy and thermocapillary three-dimensional convection at moderate Pr: Numerical study, *Comp. Fluid Dyn.* **1,** 337 (1992).
11. S. Ostrach, Low-gravity fluid flows, *Ann. Rev. Fluid Mech.* **14,** 313 (1982).
12. R. Piva, M. Strani and G. Graziani, Moti convettivi in condizioni di gravitá ridotta con superficie libera, in *VI Congr. Naz. AIDAA, Roma 15-19, Giugno, 1981* (unpublished).